THE DOORS OF THE EXTREME-UV IMAGER ONBOARD SOLAR ORBITER: FROM DESIGN TO FLIGHT.

Lionel Jacques [(1)], Aline Hermans [(1)], Jean-Philippe Halain [(1,2)], Jean-Yves Plesseria [(1)], Benoit Marquet [(1)]

[(1)] Centre Spatial de Liège, Belgium
[(2)] European Space Agency, ESTEC, Noordwijk and The Netherlands

ABSTRACT

The EUI instrument on board ESA's Solar Orbiter carries three doors designed to protect the instrument's delicate entrance filters from contamination throughout the mission. These mechanisms must withstand harsh launch and in-orbit thermal loads, ensure precise repositioning. They rely on passive end-stops, launch locks, and a single stepper motor per door. One door includes an additional intermediate occulter position for coronal imaging. Extensive modelling, including thermal, structural, contamination, and magnetic analyses, validated the mechanisms' performance. In-flight results confirm reliable operation, minimal degradation, and compliance with all mission requirements.

1 INTRODUCTION

Since its launch on February 10th, 2020, the Extreme Ultraviolet Imager (EUI) instrument onboard the ESA/NASA Solar Orbiter mission has been capturing close-up images of the Sun at each perihelion, revealing dynamic small-scale EUV phenomena such as campfires and fibrils and demonstrating high-resolution imaging performance [1]. As illustrated in Fig. 1 and 2, the EUI instrument is equipped with three door mechanisms, one for each telescope: the Full Sun Imager (FSI) and the two High-Resolution Imagers (HRI). The FSI and one HRI look in the extreme UV (HRI_{EUV}) through ultra-thin 150nm thick aluminium filters while the second HRI targets the Lyman-α ($HRI_{Ly\alpha}$) through a thick MgF_2 filter.

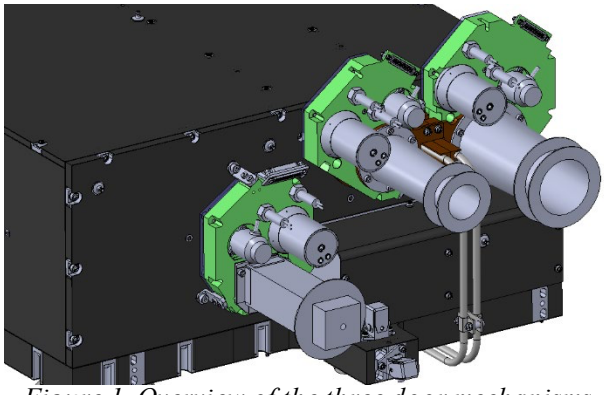

Figure 1. Overview of the three door mechanisms integrated in the instrument CAD models. From left to right: FSI, $HRI_{Ly\alpha}$ and HRI_{EUV}.

The doors are designed to protect the instrument's entrance filters from contamination, acoustic vibrations during launch, and excessive solar radiation during non-operational periods surrounding the scientific observation windows at 0.28AU [2, 3].

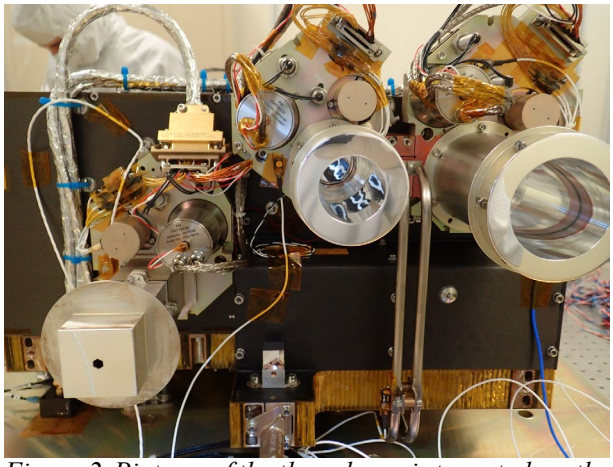

Figure 2. Pictures of the three doors integrated on the EUI flight model, during vibration test preparation.

2 DOOR DESIGN DESCRIPTION

2.1 Requirements summary

Each door includes an optical filter (specific to HRI_{EUV}, $HRI_{Ly\alpha}$, or FSI) that must remain protected from UV exposure and contamination, with the mechanism ensuring light-tightness during non-operational phases. They preserve the filter's integrity under both harsh thermal environment and acoustic launch conditions. The HRI_{EUV} and FSI doors include venting labyrinths around their entrance filter to mitigate pressure gradients during launch depressurization and purging. The FSI door accommodates an additional intermediate "occulter" position, allowing for observations of the solar corona. Since the doors remain closed during non-operational phases, ensuring their reliability throughout the mission is also essential. Finally, the doors support each their heat-rejecting entrance baffle at the front of which the pupil of the telescope is located. The pupil of the FSI channel is a 5mm wide hexagon while the pupil of both HRI channels is circular, with a diameter of 30mm and 47.4mm for the Lyα and EUV channel, respectively.

2.2 Configuration

Due to their larger entrance apertures, the HRI doors experience significant thermal load, which is managed by connecting them to a dual heat pipe system using a set of annular copper interfaces, as shown in Fig. 1 and 2. The heat pipes evacuate the heat absorbed by the door assemblies towards a dedicated spacecraft interface. The FSI door does not require a dedicated thermal interface since its pupil is much smaller.

Despite the thermal coupling between the HRI doors, all three mechanisms share a common configuration. Fig. 3 and 4 describe the door mechanism, that is based on a rotating lid, directly mounted onto the shaft of a Phytron stepper motor and is featuring several key components: reed switches for position indication, a TiNi™ pin puller for launch lock functionality, $SmCo_5$ magnets for end-stop locking and position sensing, and labyrinths for contamination protection.

Since the front panel of the EUI instrument is made of a CFRP (carbon-fibre reinforced plastics) aluminium honeycomb sandwich, isostatic mounting is mandatory to accommodate the CTE (coefficient of thermal expansion) mismatch between the aluminium door housing and front panel. The door is therefore mounted through two flexible titanium blades pointing towards the rigid mount located close to the motor to carry most of the mechanical load.

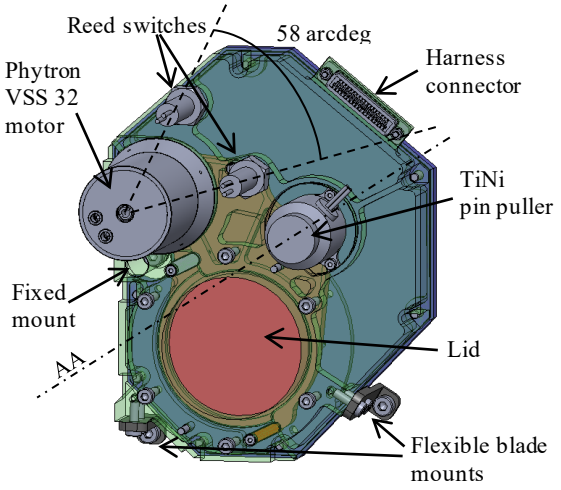

Figure 3. HRI_{EUV} door mechanism elements.

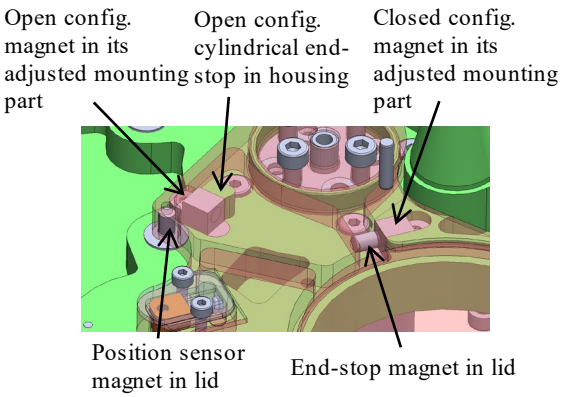

Figure 4. HRI_{EUV} door $SmCo_5$ end-stop magnets.

Fig. 5 illustrate the specific 3 positions of the FSI door, including the occulter for coronal imaging.

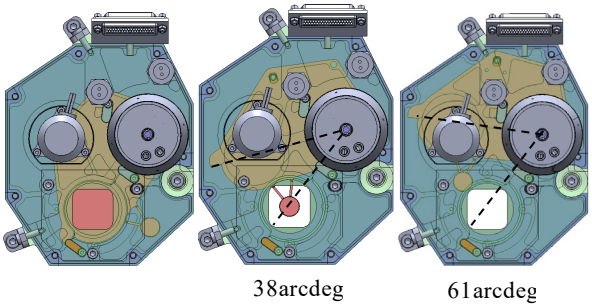

Figure 5. FSI door mechanism three positions with occulter.

2.3 Launch lock

To mitigate air motion, vibrations and shocks in the vicinity of the filter during launch, the lid is locked in its closed position to ensure no relative motion is possible. This is fulfilled by using a pin-puller. As illustrated in Fig. 6 and 7, when the spherical head pin enters the conical hole of a Vespel SP3 slider, it forces the slider to move parallel to the v-shaped notch direction. The notch is located at the far end of the lid, where the free displacements are the largest. The slider spring is preloaded such that the radial load onto the pin is lower than the operational radial load acceptable (44N). The spring free length is 9.46mm and is compressed to 8.5mm (23N) when the pin is not engaged and 8mm when it is engaged, giving 35N preload. The spring is made of 17/7 PH Stainless Steel (AMS 5678). The notch is oriented perpendicular to the movement direction such that the force is aligned with the movement. The 35N spring preload also ensures that it prevents the door from moving out of the notch during launch.

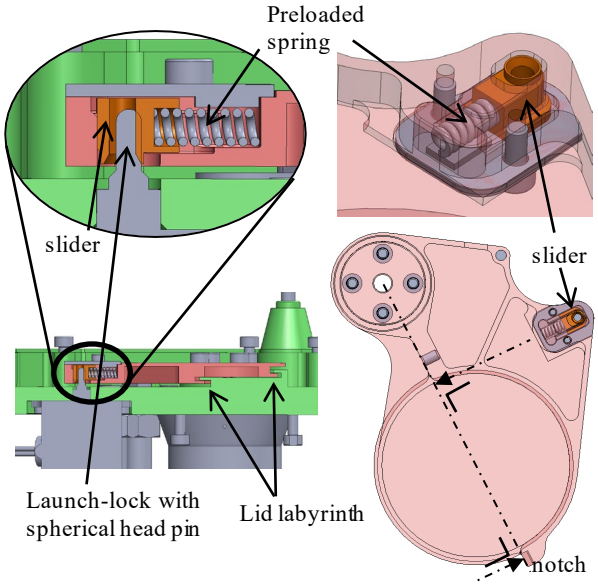

Figure 6. Left: AA plane cut view (see Figure 3) of HRI_{EUV} door mechanism with pin puller / slider / spring concept. Right: slider details and orientation.

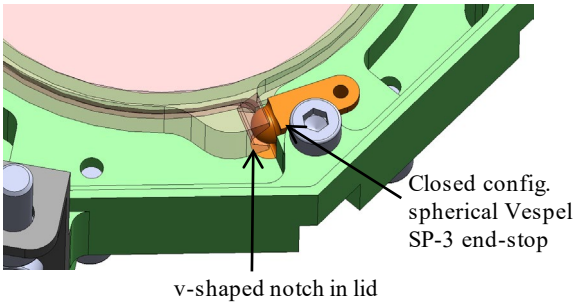

Figure 7. Backside view of the HRI_{EUV} door lid notch against the Vespel end-stop in closed configuration.

2.4 Mass budget

Including the copper interface and baffles, the mass of the door mechanism flight models was 740gr, 685gr, and 598gr for the HRI_{EUV}, $HRI_{Ly\alpha}$ and FSI, respectively.

3 MAGNET SIZING & TORQUE BUDGET

3.1 End-stop magnet sizing

Due to the presence of a magnetometer onboard Solar Orbiter, the overall instrument magnetic moment had to be minimised. NSSN configuration of the rotor magnets was specified to Phytron. To reach the required deliverable torque, $SmCo_5$ magnets were used instead of AlNiCo.

The force between two identical cylindrical magnets placed end to end at great distance ($x > R$) can be approximated through the following formula:

$$F = \frac{B_0^2 A^2 (L^2 + R^2)}{\pi \mu_0 L^2} \left(\frac{1}{x^2} + \frac{1}{(x+2L)^2} - \frac{2}{(x+L)^2} \right) \quad (1)$$

where B_0 is the magnetic flux density close to the pole, A is the cross section of the magnet, L is its length, R its radius, x is the separation between the two magnets μ_0 is the permeability of space.

Due to the close configuration of the magnets, the large air-gap assumption was not strictly valid and the value obtained with the analytical formula was refined by magnetic Finite Element Analyses (FEA) conducted in the GetDP/Gmsh software suite [8,9]. The force obtained with FEA is 0.498 [N] for the same magnet (990 [mT], 740 [kA/m]) instead of 0.423 [N], meaning less than 15% discrepancy.

The contribution of all small magnets for end-stop securing and occulter positioning was taken into account in the overall instrument magnetic moment.

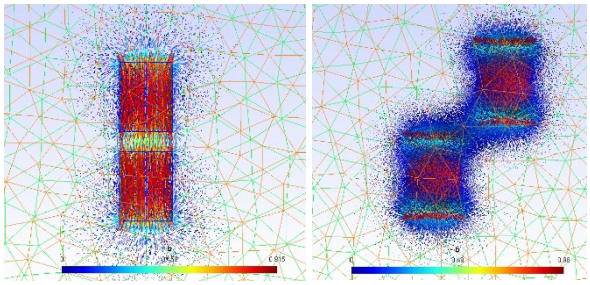

Figure 8. FEA magnet force modelling for end-stop and occulter positioning.

3.2 Occulter magnet sizing

The requirement is to keep the FSI occulter within ±0.25 arcdeg of the centred position. To ensure accurate positioning of the FSI occulter when the motor is unpowered, two supplementary $SmCo_5$ magnets are integrated to compensate for possible step losses (up to 2 steps or 3.6 arcdeg) and detent torque (3 mNm). The selected magnets are 2.95 mm in diameter and 3.85 mm long, exhibiting a worst case coercivity of 740 kA/m. With a 1.4mm air gap between them, they generate a torque greater than the detent torque across the full misalignment range, (up to 12 mNm) to realign the occulter within specification, despite generating lower absolute force than the end-stop magnets. The increased torque is due to the greater radius (63 mm vs. 22 mm for end-stops), confirming the design's adequacy for guiding the occulter passively into position. Fig. 9 shows the resulting torque profile for the FSI door, exhibiting a peak at 12mNm.

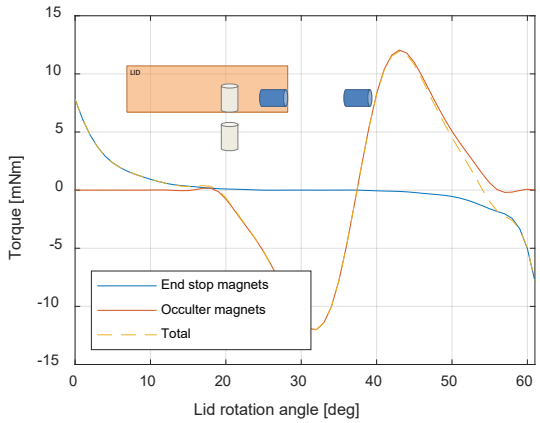

Figure 9. FSI lid torque due to magnets.

3.3 Torque budget

Torque budget was computed according to ECSS [7], including the prescribed uncertainty factors. Tab. 1 summarises the different contributors, with a minimum deliverable output torque of 41mNm.

Table 1. Torque budget [mNm].

	$HRI_{Ly\alpha}$	HRI_{EUV}	FSI
Magnets	8.2	10.8	12.0
Friction @-30°C	1.7	1.7	1.7
Gravity	7.1	9.7	5.5
Acceleration	0.01	0.02	0.01
On-ground	17.0	22.2	19.2
In-orbit @-30°C	29.6	37.5	41.1

While the motors were specified to deliver at least 43mNm, the FM motor measured running torque at nominal current (600mA) was eventually 70mNm.

4 CONTAMINATION MANAGEMENT

4.1 External contamination mitigation

To prevent external contamination from reaching the filter, a radial labyrinth is foreseen with the lid in the closed position all around aperture. Because of the lid kinematics, the labyrinth is divided in two parts, one on each side of the radius passing through the rotation axis and the aperture centre. On one side, the male part of the labyrinth on the lid is going away from the aperture centre. On the other side, it goes towards the aperture centre. The labyrinth is highlighted in Fig. 6. The clearance in the labyrinth, compatible both with venting requirements and relative displacements during vibration, gives an axial gap of 0.2mm with a radial gap of 0.5mm.

4.2 Lubricant evaporation analysis

The main source of contamination being the bearing lubricant, the motor temperature profile throughout the mission was first estimated and is shown in Fig. 10. As they are the hottest, only the HRIs were computed since the vapour pressure of the lubricant increases with temperature and so does the contamination. It is important noting that the temperature of the motor is directly influenced by the lid temperature in closed position. The hotter the lid, the hotter the rotor and bearings. Insulating washers were therefore integrated between the lid and the motor shaft flange, as illustrated in Fig. 11.

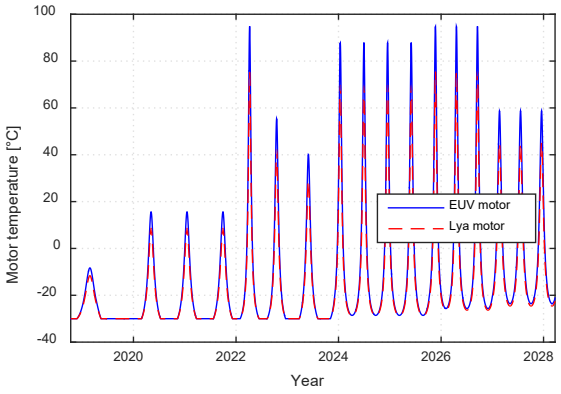

Figure 10. Evolution of the HRI motor temperature over the mission.

To mitigate contamination from the motor, a labyrinth was designed at the interface between the lid and the housing.

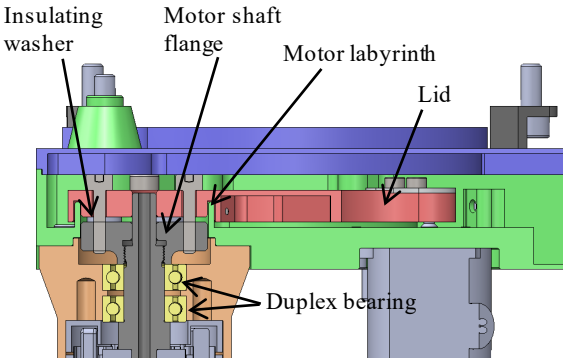

Figure 11. Labyrinth geometry around the HRI_{EUV} motor flange.

The computation is performed according to the formula recommended in [4]. This formula gives the total evaporation through an output gap based on material properties, temperature, duration and geometry. To define the gap/labyrinth, the geometry is unfolded to simplify the design in a simple annular duct defined by its mean diameter (d), its gap (b) and its length (l). The two ducts (in the motor and the housing) are placed in series and the labyrinth in the housing is unfolded.

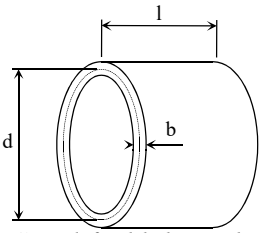

Figure 12. Simplified labyrinth modelling.

The conductance through the duct in molecular regime is given by:

$$C = \frac{\pi d b V}{4 + 1.5 l/d} \qquad (2)$$

where $V = \sqrt{\frac{8k_B T}{\pi m}} = \sqrt{\frac{8RT}{\pi M}}$. The flow through the duct is then determined by $Q = C\,P$ [Pa/m^{3}s] leading to the mass flow rate $Q' = Q\frac{M}{RT}$ [mg/s].

$$Q' = \sqrt{\frac{8}{\pi R}} \frac{P\pi d b \sqrt{\frac{M}{T}}}{4 + 1.5 l/b} = 0.436 \frac{P\pi d b \sqrt{\frac{M}{T}}}{1 + 0.375 l/b} \qquad (3)$$

with Q' in mg/s, P in mbar, d,b,l in mm, M in g/mole and T in K. Note that the units are important and define the coefficient.

The mass flow rate is then multiplied by the duration to assess the total amount of evaporated lubricant, assuming infinite source.
Previous equation highlight that the most relevant physical parameters are the molar mass and the vapour pressure (as a function of temperature). While the molecular mass is quite well known (and of low impact on results), the vapour pressure as a function of temperature faces very variable measurements which may have impact of several orders of magnitude. A review of available data and measurements was performed in the frame of the Sentinel 4 UVN project. Fig. 13 shows the different data collected for the Fomblin Z25 and the Castrol Braycote 815Z. Values found in Castrol datasheet appears to be the most realistic for Braycote 815Z and ECSS/ESA data were considered as more conservative for the Fomblin Z25. Fitting the data with the Clausius-Clapeyron law, recalled in Eq. 4, is shown Fig. 14.

$$P(T) = P\left(T_{ref}\right) e^{\frac{L}{R}\left(\frac{1}{T_{ref}} - \frac{1}{T}\right)} \qquad (4)$$

Combining conductance given in Eq. 3 with vapour pressure fit and motor temperature profile eventually gives the lubricant mass flow rate through the labyrinth over the mission lifetime. Fig. 15 illustrates the results and highlights that the Braycote, due to its lower vapour pressure, induces less lubricant migration.

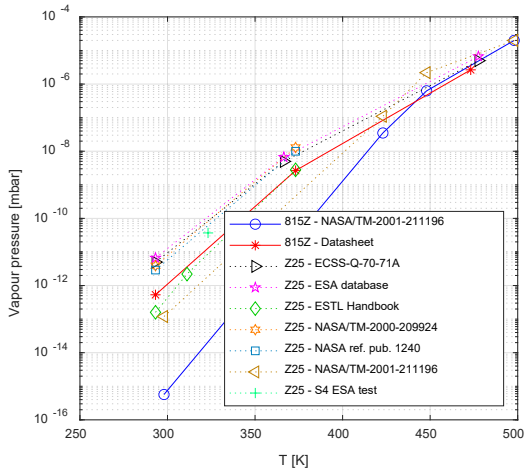

Figure 13. Vapour pressure datasets in function of temperature for Fomblin Z25 and Braycote 815Z.

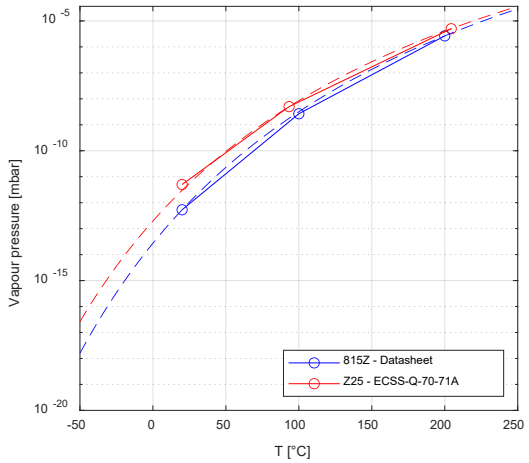

Figure 14. Clausius-Clapeyron fit of Braycote 815Z and Fomblin Z25 vapour pressure.

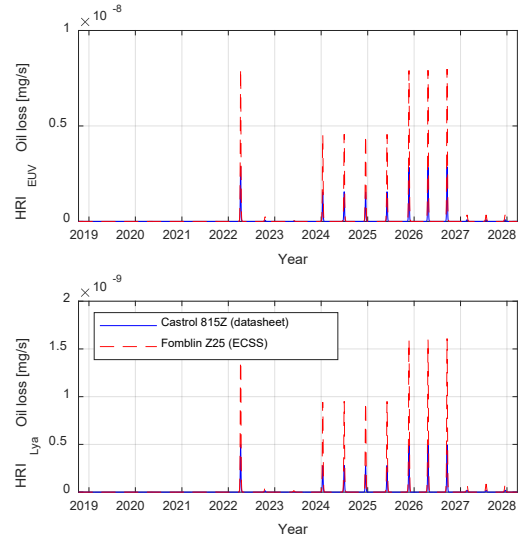

Figure 15. Evaporation rate in both HRIs over the mission lifetime.

Tab. 2 summarises the lubricant evaporation analysis results for the most critical channel $HRI_{Ly\alpha}$.
The required maximum contamination onto the filter is 0.37µgr/cm². The door mechanism internal cavity surface area is approximately 200cm² for the $HRI_{Ly\alpha}$ door. Assuming that the contamination will spread uniformly into the cavity (this is a worst case since the filter is the hottest part in the door mechanism when it is open), the total lubricant loss over the entire mission is 0.74mg for and $HRI_{Ly\alpha}$. Taking much more stringent assumptions, with all the lubricant going to the filter, the requirement become 2.6µg.

Table 2. $HRI_{Ly\alpha}$ lubricant evaporation analysis.

		HRI_{Lya}		
		Requirement [µg]	Evaporated mass [µg]	MoS
Whole cavity	815Z	74	2.0	36.1
	Z25		7.0	9.5
Filter only	815Z	2.6	2.0	0.31
	Z25		7.0	-0.63

Slightly negative margin of safety was obtained only when considering that all the evaporated lubricant goes to the filter. In this case, only the Braycote datasheet gave positive margin of safety for the Lyα filter. In the more realistic case where the evaporated lubricant is spread all over the door cavity, margin of safety was largely positive. The calculations were done using conservative and pessimistic assumptions: all oil escaping the motor is sticking on the surface cavity and remains there until end of mission. In reality:

- there is a large path to space when the door is open;
- evaporated oil won't be distributed uniformly over the door cavity but will be collected preferentially by the coldest part and the filter is not the coldest part;
- S/C heat shield doors closed cases are being ignored;
- End-of-life coating properties are assumed throughout the mission lifetime to compute the temperatures;
- evaporated mass and margins of safety are computed at the end of the extended mission.
- motor were requested to be baked-out.

Based on the above analysis, wet Braycote lubricant was preferred over the suggested dry lubricant (MoS_2).

5 MECHANICAL ANALYSES

5.1 Finite element model overview

Fig. 16 shows a global view of the HRI door mechanisms finite element (FE) mesh. The $HRI_{Ly\alpha}$ is on the left and the HRI_{EUV} is on the right of the figure. They are mechanically linked by the thermal interface. Only the reed switches were modelled as lumped masses as well as the harness connector (connected to the bracket at the top of the doors). The different parts are linked by their respective screws, modelled as rigid by elements. This allows not only to better represent the assembly but also to retrieve the load in each fastener for subsequent analysis. The FSI door FE model was done similarly.

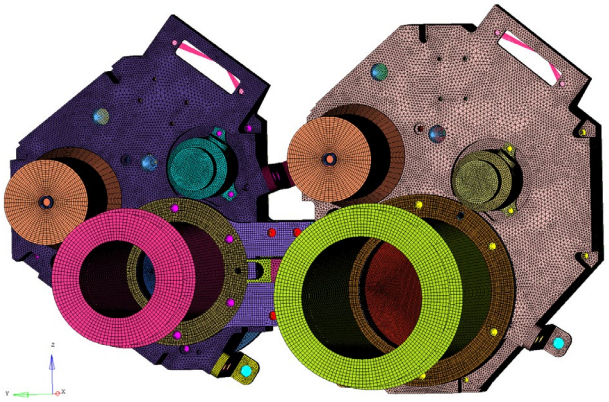

Figure 16. FE mesh of the HRI doors.

5.2 Lid and motor modelling

To mitigate the risk of shocks in the vicinity of the filter, accurate modelling of the lid was required. Fig. 17 shows the details of the three lid boundary conditions:

1. It is mounted onto the motor flange (fixed itself onto the shaft & rotor) through 4 M3 bolts. It is free to rotate around the motor axis in this point.
2. At the TiNi™ pin puller location, it was assumed rigidly linked to the TiNi™ pin in the plane of the lid but free in the direction of the pin. This model was correct as long as the reaction on this point in the direction of the spring is lower than the preload in the spring. The reaction was then extracted from the FE model to check this assumption.
3. At the notch location, the lid was kept free to move in the plane of the lid but rigidly linked to the housing in the direction parallel to the rotation axis. Forces in this link were also extracted from the FE model results.

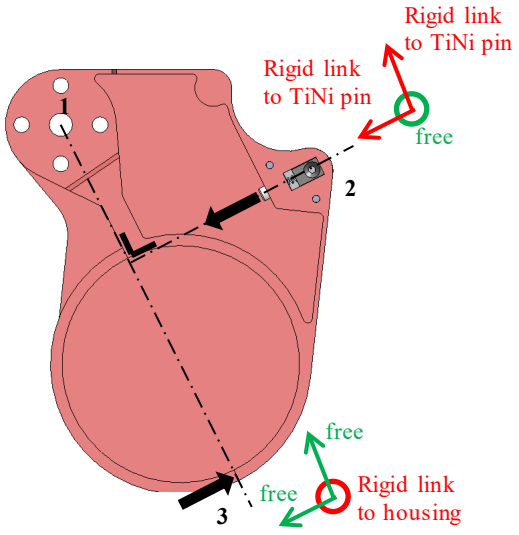

Figure 17. Lid mechanical model connection details.

To ensure proper shaft stiffness representativity, the motor was modelled in detail with its internal components. The duplex ball bearing was composed of two GRW SS688/003-2Z bearings made of X65Cr13 stainless steel. The bearings were mounted in O configuration. The radial clearance was 8µm giving a contact angle of 10.8deg. According to Phytron, the preload of the duplex bearing was around 10N. The single bearing at the end of the shaft was a GRW SS624/0003-2Z also made of X65Cr13 stainless steel (both rings and balls). The stiffness of the ball bearings was computed with CABARET and introduced in the FE model though a bearing link between the external ring and the internal ring (one link for the duplex and one link for the single bearing).

5.3 Results

Static, random, thermos-elastic and shock analyses were conducted. At critical design review, the first mode of the HRI door assembly was expected at 467Hz while the FSI was around 473Hz. Qualification and flight model vibration testing showed that the actual first eigen frequency was around 530Hz for the HRI door assembly and 570Hz for the FSI.
Positive margins of safety were obtained for stresses, fasteners and lid gapping analysis. The maximum axial displacement of the lid is 229 µm, which remains within the effective labyrinth clearance of 260 µm (accounting for manufacturing and assembly tolerances). Since launch occurs at ambient temperature, no additional thermo-elastic effects apply. The nominal radial gap of 500 µm, reduced to 190 µm due to tolerances, also maintains sufficient margin, with random vibration-induced radial displacements reaching only 36 µm.

6 THERMAL ANALYSES

6.1 Introduction

The doors together with the entrance baffle are directly exposed to the 13 solar constants (SC) at perihelion. They are partially protected by the spacecraft heat shield, itself equipped with doors. Most of the door being made of aluminium except for the motor, most of the gradient was expected between the tip of the entrance baffle and the door housing. In closed position, the lid is only connected through the ball bearings and driving their temperature and lubricant evaporation potential as discussed in Sec. 4. The lid was thermally insulated from the motor shaft using four Vespel SP3 washers to reduce conductive heat transfer, which helps limit the bearing temperature but leads to increased lid temperature. Nevertheless, it seemed critical to assess the thermal conductance of the ball bearings.

6.2 Conduction through ball bearings

First, the bearing conductance was calculated using Hertzian contact theory [5, 6], assuming dry conditions for conservativeness. It resulted in a total conductance of 0.0236 W/K for the duplex bearing, neglecting the single bearing which had almost no preload. In addition, a dedicated thermal balance test of the motor was conducted to better estimate the actual conductive path through the bearings. Using a controlled heating setup, injecting heat on the rotor interface, the test showed that conductance increases with temperature as illustrated in Fig. 20 and 21. The measured conductance at ambient temperature was approximately 0.03 W/K. These values were used to update the thermal model for improved accuracy in motor temperature predictions.

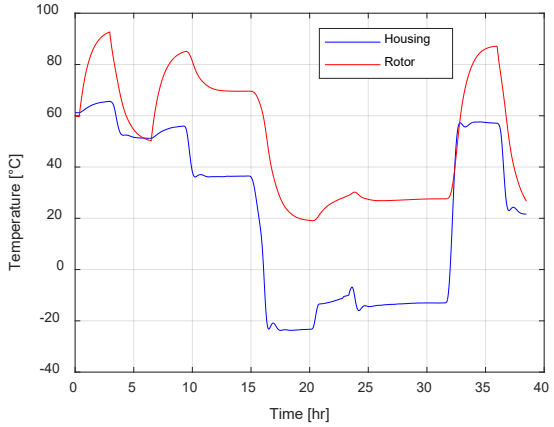

Figure 18. Rotor/stator conductance test, showing the temperature of the housing and the rotor.

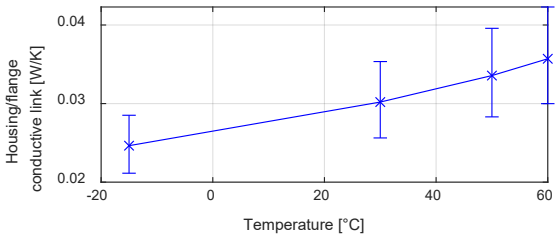

Figure 19. Thermal conductance between stator and rotor evolution as function of the temperature.

6.3 Results

The thermal analysis of the EUI door mechanisms was conducted in ESATAN-TMS and based on detailed thermal models integrated within the full instrument model. It considered various mission phases: hot and cold cases, with doors either open or closed, in both operational (OP) and non-operational (NOP) modes. With a S/C interface of the heat pipe at 50°C, results showed that in the hot case, the HRI_{EUV} lid reached up to 164°C (still below the 200°C qualification temperature of the heat rejection coating of the lid), with significant thermal gradients in the motor and bearings, as presented in Fig. 20. The FSI door experienced lower and more uniform temperatures due to its smaller aperture.

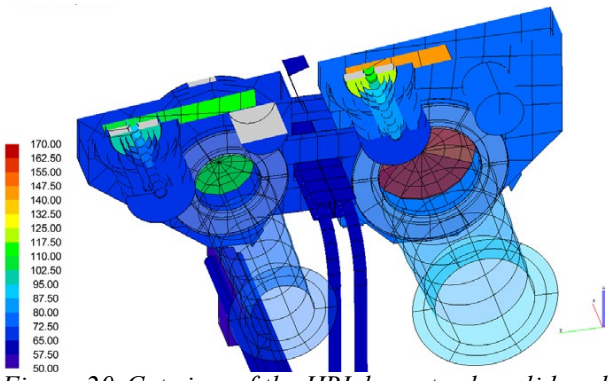

Figure 20. Cut view of the HRI doors to show lid and motor temperature.

After assembly in ISO5 cleanroom, the thermal design was validated through environmental qualification and thermal balance tests with 13 solar constants collimated sun simulator.

7 IN-FLIGHT RESULTS

Fig. 21 shows the in-flight temperature of the HRI_{EUV} door lid and motor during three consecutive perihelia. The plots highlight the correlation between the motor and lid, the motor housing being hotter each time the door is opened. The lid rejecting more heat than the filter, the door assembly is generally colder when the door is closed, and more heat is directly rejected to space. The figure also shows that the lid temperature tends to increase over the presented 3 perihelia, gaining around 15°C with a constant S/C interface temperature, indicating a potential increasing absorption of the lid coating.

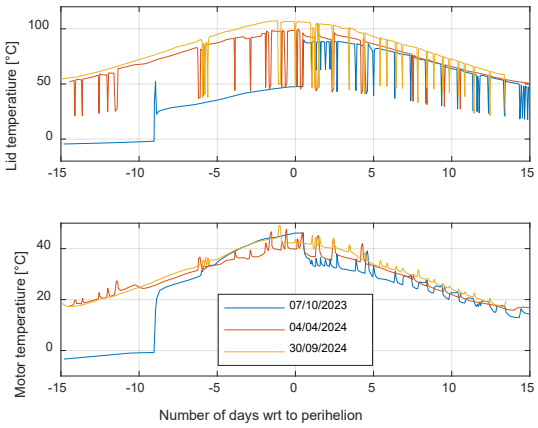

Figure 21. HRI_{EUV} lid and motor temperature, during the 07/10/2023, 04/04/2024 and 30/09/2024 perihelia.

The in-flight success of the FSI door in occulting mode led to a demand for more actuation than initially expected. The qualification model of the door was thus subjected to an additional actuation qualification to confirm there would be no risk in actuating more the mechanism in coronal imaging mode.

8 CONCLUSIONS

The EUI door mechanisms fulfil all mission requirements for thermal, mechanical, and contamination performance. Each door variant was optimized for its specific aperture and filter accommodation while maintaining a modular, robust design. Extensive analyses and testing confirmed compliance with load cases, thermal margins, and repositioning accuracy. The occulter positioning system on FSI performed successfully, enhancing science data quality. In-flight use during perihelion validated the mechanisms' reliability and stability. Since its launch in 2020, the doors are performing successfully.
Based on the successful EUI door heritage, CSL is selected to design the two doors of the Joint EUV coronal Diagnostic Investigation (JEDI) instrument aboard the European Space Agency's Vigil space weather mission.

9 REFERENCES

1. D. Berghmans, *et al.* (2021). Extreme-UV quiet Sun brightenings observed by the Solar Orbiter/EUI, *Astronomy & Astrophysics (A&A)* **656**(L4).

2. Rochus P., *et al.* (2020). The Solar Orbiter EUI instrument: The Extreme Ultraviolet Imager, *Astronomy and Astrophysics*, **642**(8).

3. Jacques L., *et al.* (2011). Ultrathin EUV Filters Testing and Characterization under High Flux (13 SC) for Solar Orbiter EUI Instrument. *Proceedings of the 62nd International Astronautical Congress*.

4. ESTL Space Tribology Handbook

5. Lewis, S. D. (1995). Cabaret - a new software tool for analysis of solid-lubricated ball bearings in space applications, *6th European Space Mechanisms and Tribology Symposium*, **374**, 393.

6. Takeushi Y. R. (2006). Influence of Oil Lubrication on Spacecraft Bearing Thermal Conductance, *Proceedings of the 38th Aerospace Mechanisms Symposium*, Langley Research Center.

7. ECSS-E-ST-33-01C Space engineering, mechanisms

8. Dular P., Geuzaine C. *et al.* (1999). An Evolutive Software Environment for Teaching the Finite Element Method in Electromagnetism. *IEEE Transactions on Magnetics*, **35**(3): 1682-1685

9. Geuzaine C. and Remacle J.-F. (2009). Gmsh: a three-dimensional finite element mesh generator with built-in pre- and post-processing facilities. *International Journal for Numerical Methods in Engineering* **79**(11), 1309-1331.